

Label-free field-effect-based single-molecule detection of DNA hybridization kinetics

Sebastian Sorgenfrei, Chien-yang Chiu, Ruben L. Gonzalez, Jr., Young-Jun Yu, Philip Kim, Colin Nuckolls, Kenneth L. Shepard

1. Fabrication of devices
2. Lifetime histograms with probe DNA NH₂-5'-GGAAAAAAGG-3' (Device 1)
3. Measurements with probe DNA NH₂-5'-GTGAGTTGTT-3' (Device 2)
4. Lifetime histograms with probe DNA NH₂-5'-GTGAGTTGTT-3' (Device 2)
5. Control experiment with a non-functionalized device
6. Scanning gate microscopy (IV)
7. Control experiments with probe DNA NH₂-5'-GGAAAAAAGG-3' with complementary and non-complementary target DNAs, respectively
8. Melting curves with UV-Vis
9. Noise
10. Bandwidth of nanotube device
11. Ergodicity
12. Kinetic modes

1. Fabrication of devices

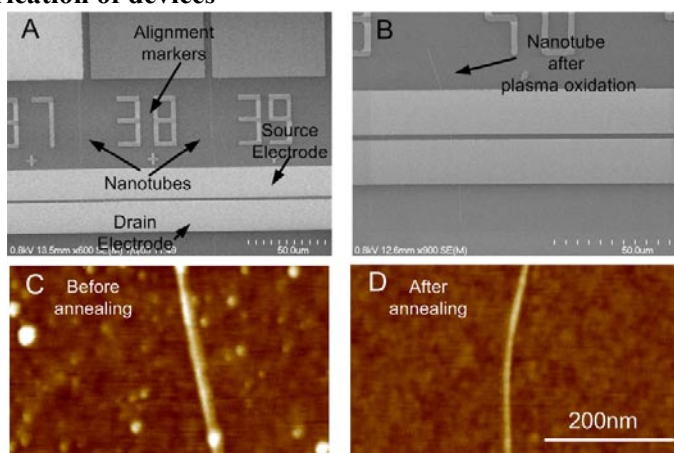


Figure S1. (A) SEM image of SWCNTs on substrate with titanium electrodes and alignment markers. (B) Electrically isolated remaining nanotube after oxygen plasma etch. (C) AFM image of nanotube after fabrication with resist residue (D) Cleaned nanotube after hydrogen/argon anneal

2. Lifetime histograms with probe DNA NH₂-5'-GGAAAAAAGG-3' (Device 1)

In order to extract the kinetics of the real time data (Fig. 2c) we have used the vbFRET software using a hidden Markov model to convert the raw conductance levels into an idealized two-level conductance. To reduce random drift, we have split the data into 15-

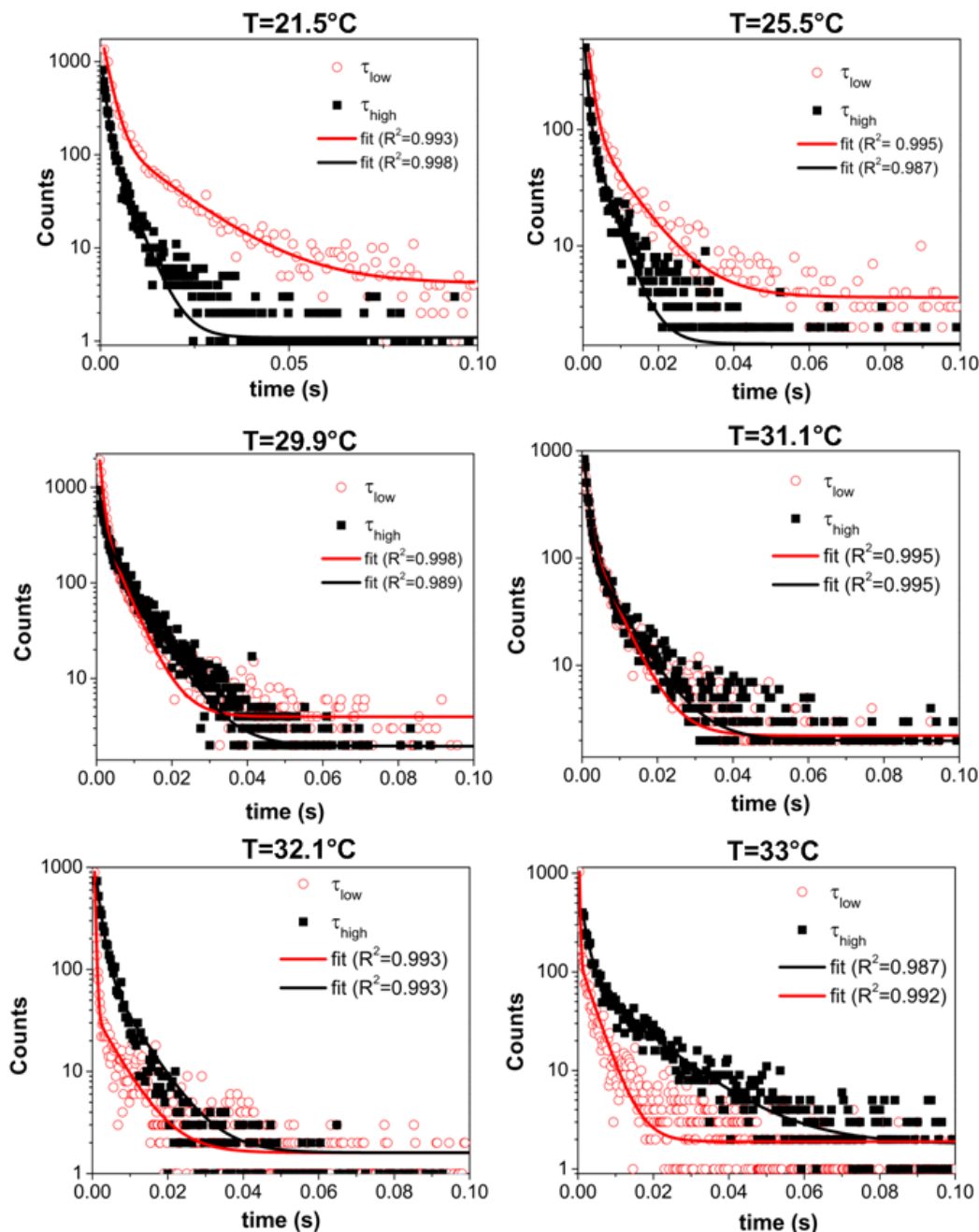


Figure S2. Kinetics analysis for device in Fig. 2. The idealized conductance traces from vbFRET are fit to a single exponential and then used for the Arrhenius plot in Fig. 4e.

second intervals and fit the data to a two-level model (a sample fit can be seen in Fig. 4a). These idealized traces are then used to extract the dwell times in the high and low states by generating dwell time histograms at each temperature (shown in Fig. S2), which can be fit to an exponential of the form $y = y_0 + A^{fast} e^{-\frac{t}{\tau^{fast}}} + A^{slow} e^{-\frac{t}{\tau^{slow}}}$. The superscript fast indicates the shorter and slow the longer lifetime of the fit, such that $\tau_{high}^{fast} < \tau_{high}^{slow}$ and $\tau_{low}^{fast} < \tau_{low}^{slow}$ (the R^2 values of the fits are always greater than 0.97). The subscripts high and low are used to indicate the lifetime of the high and low states respectively. The extracted lifetimes are used to generate the Arrhenius plot in Fig. 4e (where $k_{melting} = \frac{1}{\tau_{low}^{fast}}$ and $k_{hybridizing} = \frac{1}{\tau_{high}^{fast}}$).

3. Measurements with probe DNA NH₂-5'-GTGAGTTGTT-3' (Device 2)

We have also measured the conductance with the probe DNA NH₂-5'-GTGAGTTGTT-3'. Fig. S3 shows the current-voltage characteristics for Device 2. For the same device, the top two graphs in Fig. S4A show the conductance before exposure to complementary target DNA; the other graphs show conductance as a function of temperature after exposure to 1 μ M of complementary target DNA. Again, we have extracted the melting curve from the Gaussian fits to the two levels, shown in Fig. S4B.

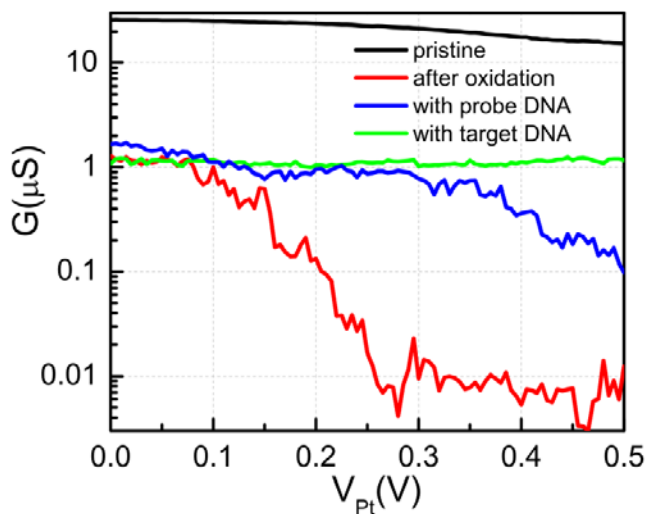


Figure S3. Conductance vs. Pt electrode at different stages for device in Fig. S4

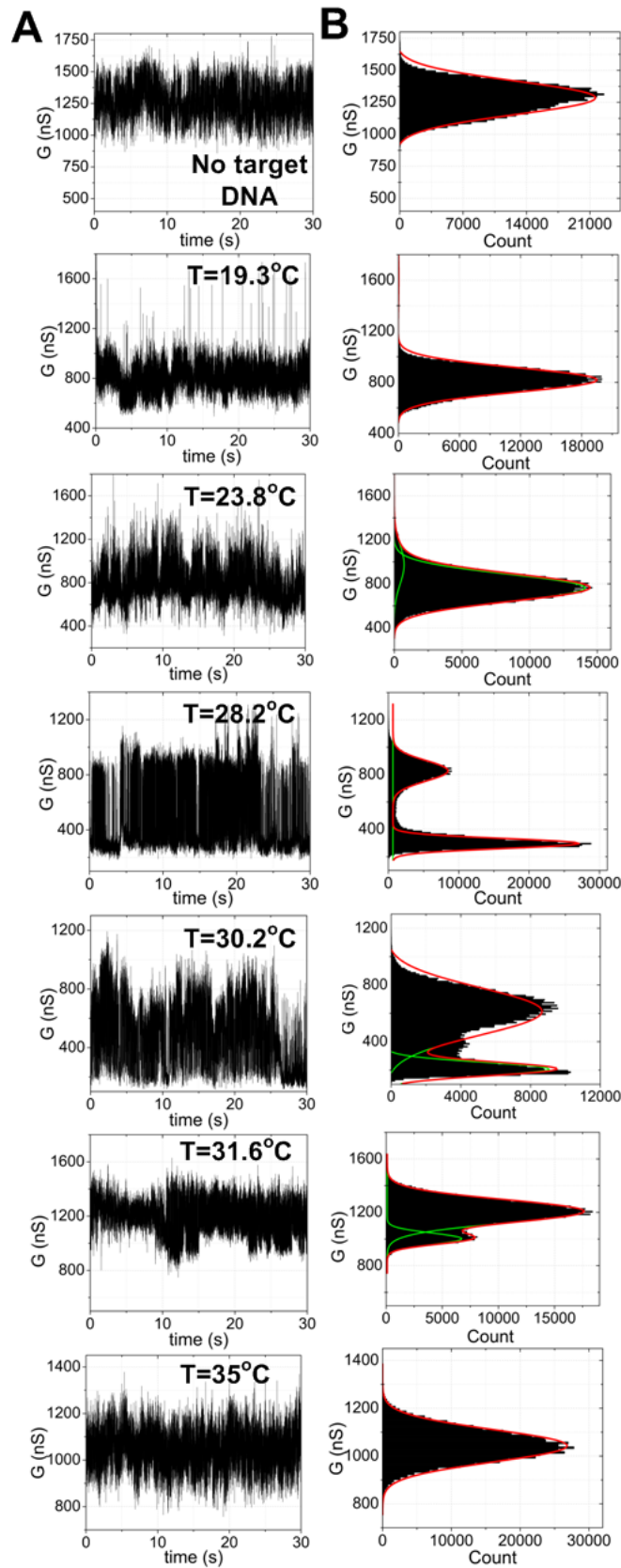


Figure S4. Conductance recordings for a nanotube device functionalized with probe DNA NH₂-5'-GAGTGTTGTT-3' with and without exposure to 1 μM complementary target

4. Lifetime histograms with probe DNA NH₂-5'-GTGAGTTGTT-3' (Device 2)

The lifetime histogram for Device 2 (real time conductance is shown in Fig. S4) is also extracted using the vbFRET software¹. The histograms and fits are shown in Fig. S5 and

have an R² value of at least 0.97 (where $k_{melting} = \frac{1}{\tau_{low}^{fast}}$ and $k_{hybridizing} = \frac{1}{\tau_{high}^{fast}}$).

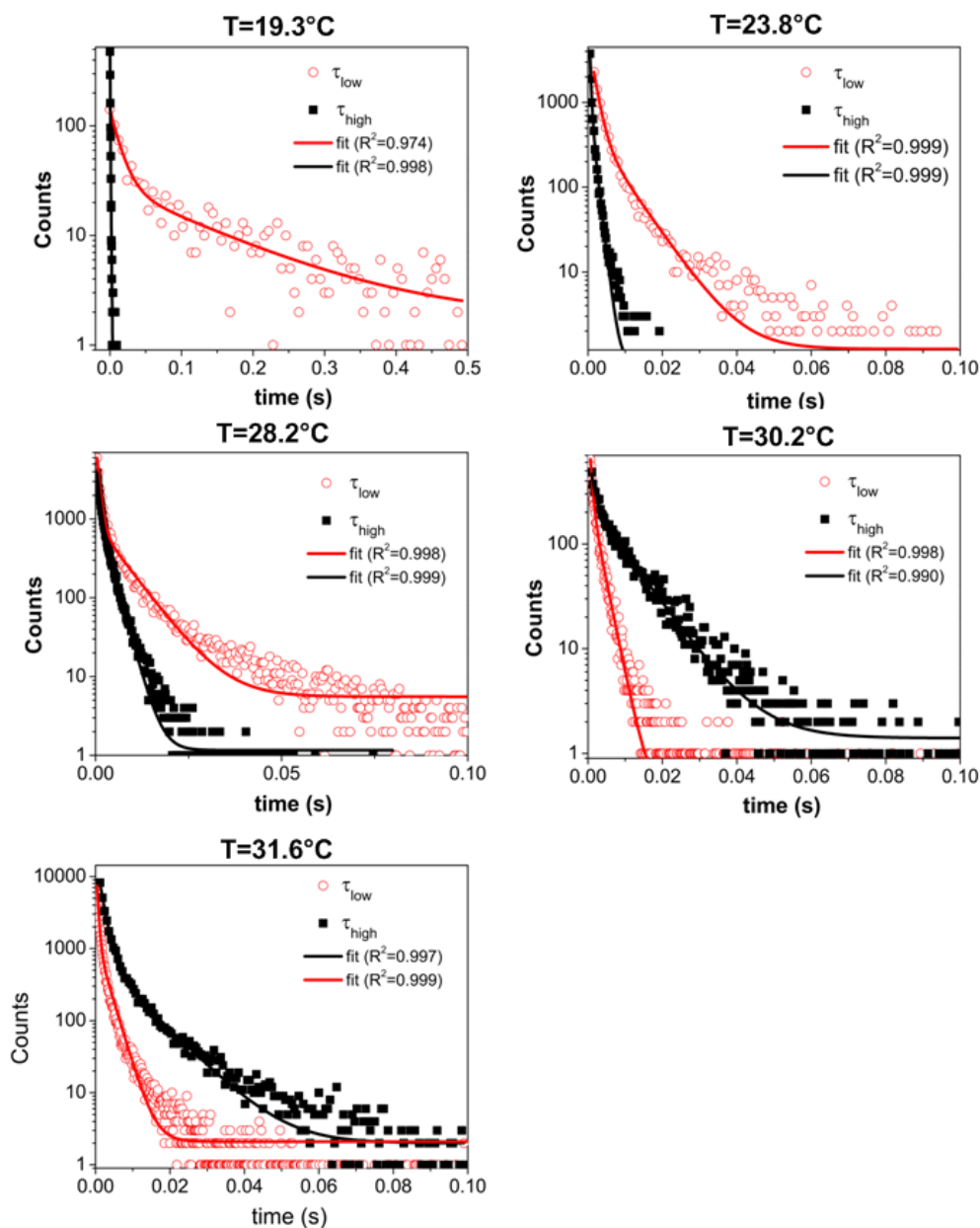


Figure S5. Kinetics analysis for device in Fig. S5. The idealized conductance traces from vbFRET are fit to a single exponential and then used for the Arrhenius plot in Fig. 4f

5. Control experiment with non-functionalized device

We have also monitored a device that has not been point functionalized. This is the same

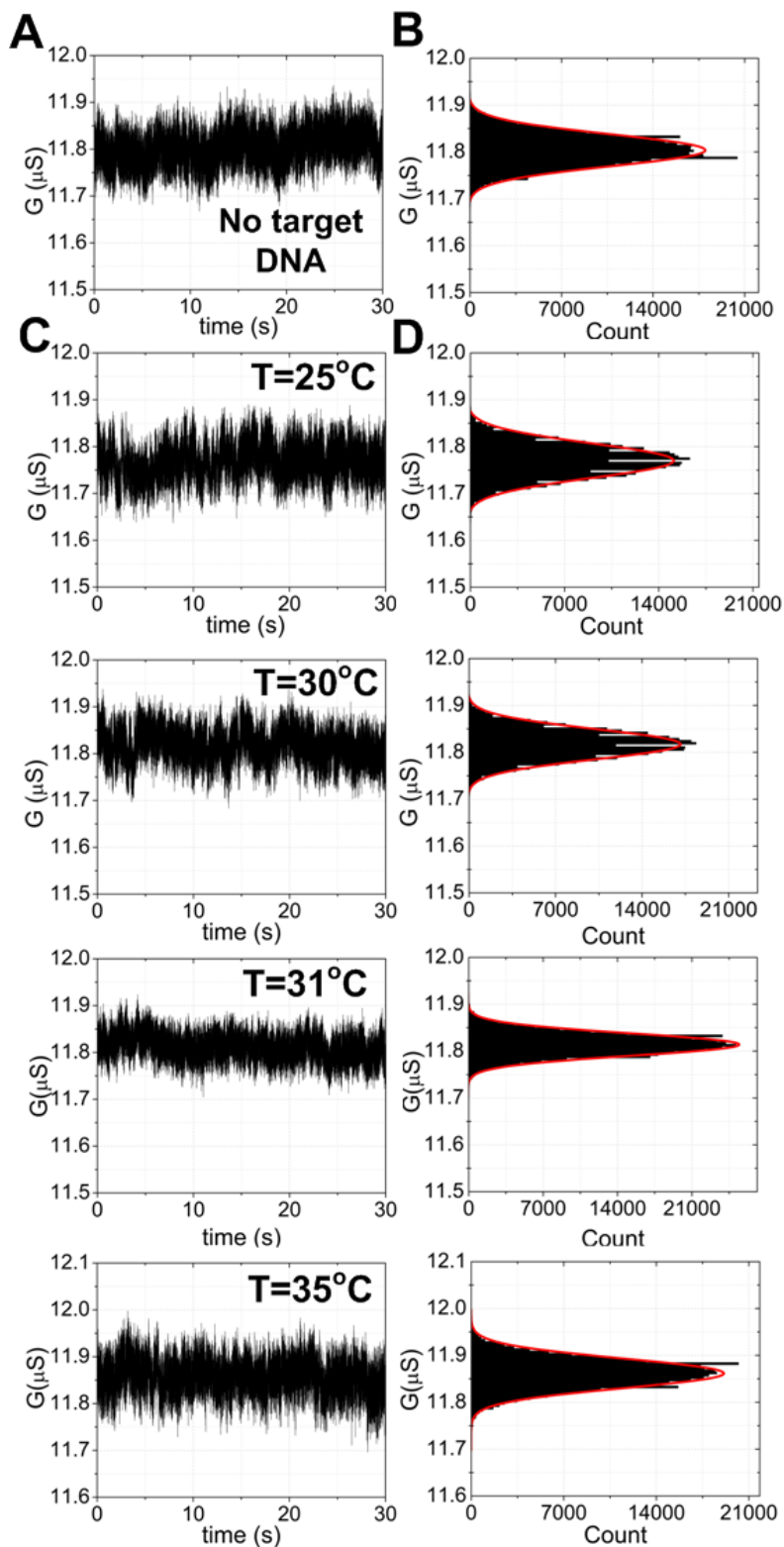


Figure S6. Real time conductance of nanotube device, which has not been point functionalized.

nanotube used in Fig. 2 (Device 1) but a different device (different electrodes). This device is exposed to 1 M $\text{H}_2\text{SO}_4(\text{aq})$ and 6.5 mM $\text{KMnO}_4(\text{aq})$ but no electrochemical potential has been applied. The conductance as a function of Pt gate voltage remains virtually identical and the device shows no significant change after overnight coupling in probe DNA and then when exposed to target DNA (Fig. S7). We have measured this device at the same time as the one in Fig. 2 and there are no two-level fluctuations at any temperature. We note here that even though the interface voltage from the solution to the platinum voltage might change, the pristine device is metallic and therefore not sensitive to small changes in electrolyte potential.

6. Scanning gate microscopy

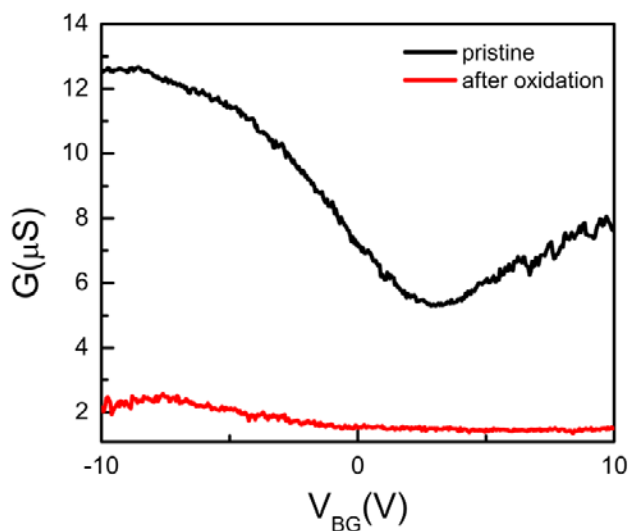


Figure S7. Conductance as a function of back-gate voltage for device used for SGM before and after oxidation. The conductance modulation due to the Schottky barrier for the pristine device can be clearly seen.

7. Control experiments with probe DNA $\text{NH}_2\text{-5'-(GGAAAAAAGG-3'}$ with complementary and non-complementary target DNAs

To confirm that the temperature correlated two level fluctuations come from the addition of complementary target DNA, we have performed the kinetics experiment with non-complementary target DNA. When no target DNA is added, there is no obvious fluctuation showing up (Fig. S8A&B). After adding the complementary target DNA, evident fluctuations appear as shown in Fig. S8C. Rinsing thoroughly the device with DI

water and buffer solution, no temperature-correlated fluctuations are observed. After adding non-complementary DNA, also no temperature correlated fluctuations are observed.

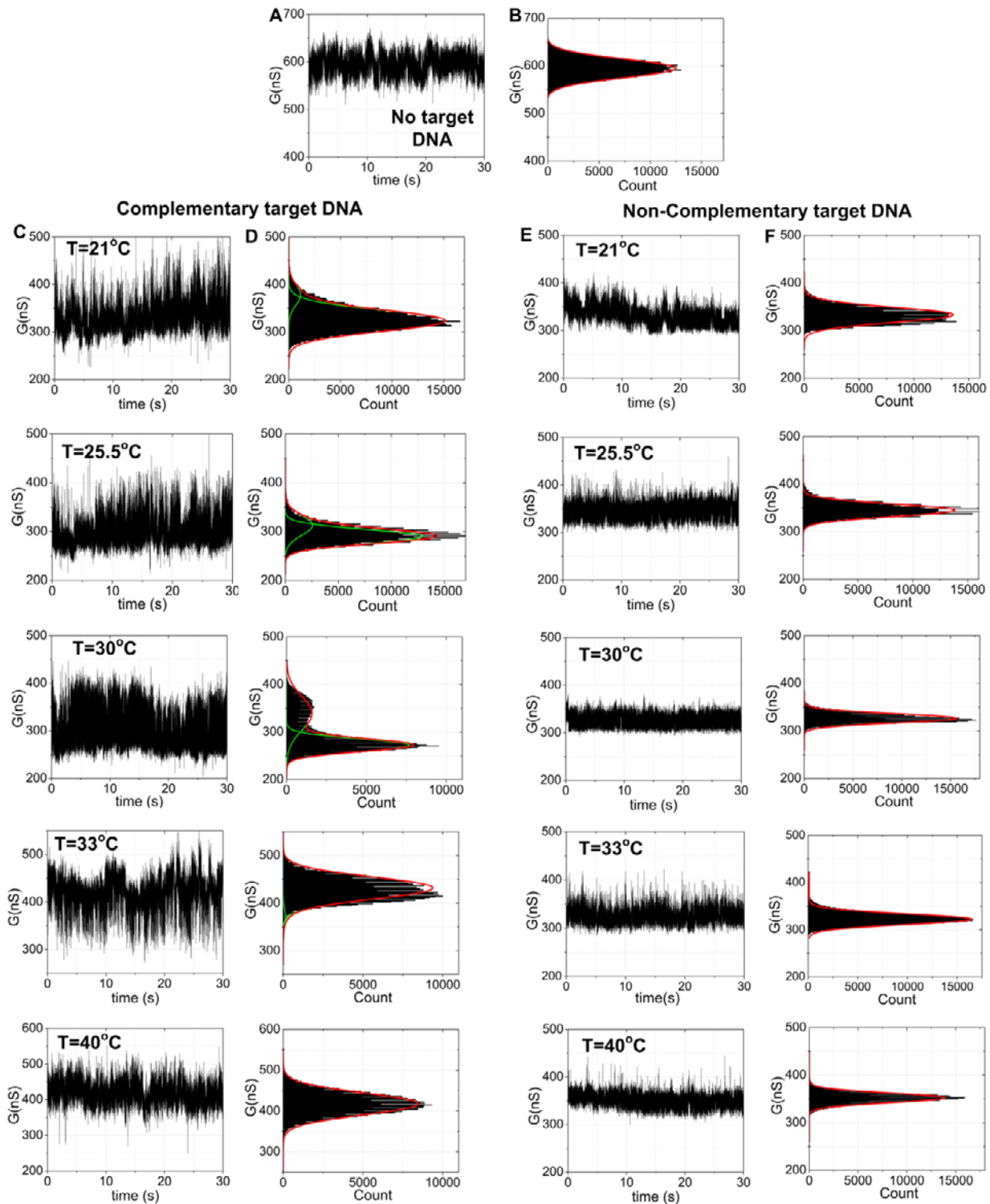


Figure S8. (A) Probe-functionalized device with no target and (B) its histogram, (C) with complementary target DNA and (D) its histogram, and (E) with non-complementary target DNA and (F) its histogram.

8. Melting curves with UV-Vis

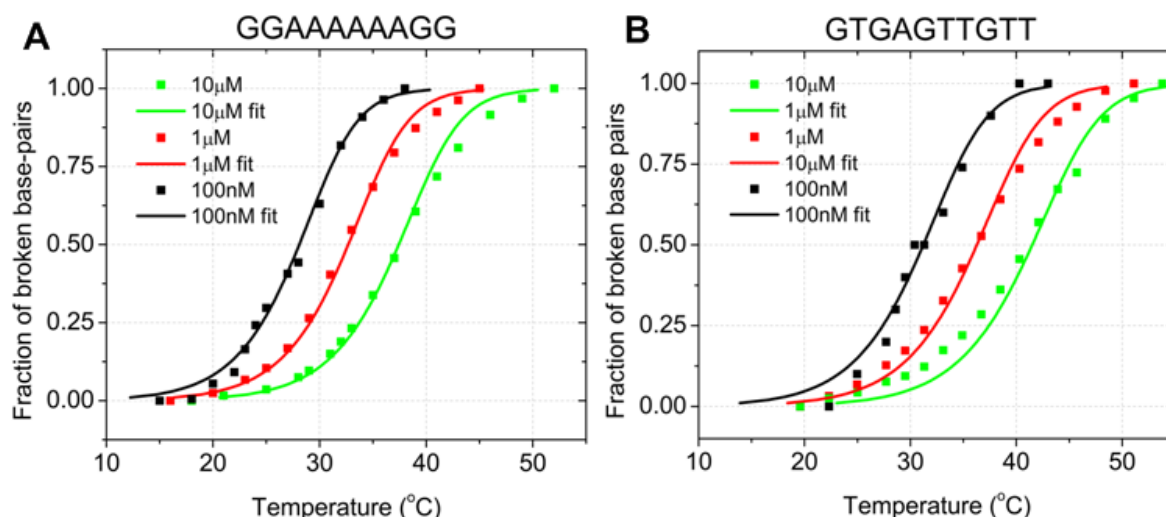


Figure S9. (A) Melting curves for probe DNA sequence NH₂-5'-GGAAAAAAGG-3' and complementary target. (B) Melting curves for probe DNA sequence NH₂-5'-GTGAGTTGTT-3' and complementary target.

The bulk melting curves for the two different DNA duplexes studied here are taken using a Shimadzu 1601 UV-Visible spectrophotometer. The temperature was maintained with a circular heater/refrigerator and was monitored with a thermocouple. We measured melting curves at three different duplex concentrations (100 nM, 1 μM and 10 μM) and extracted entropy and enthalpy using the van't Hoff equation.

9. Noise

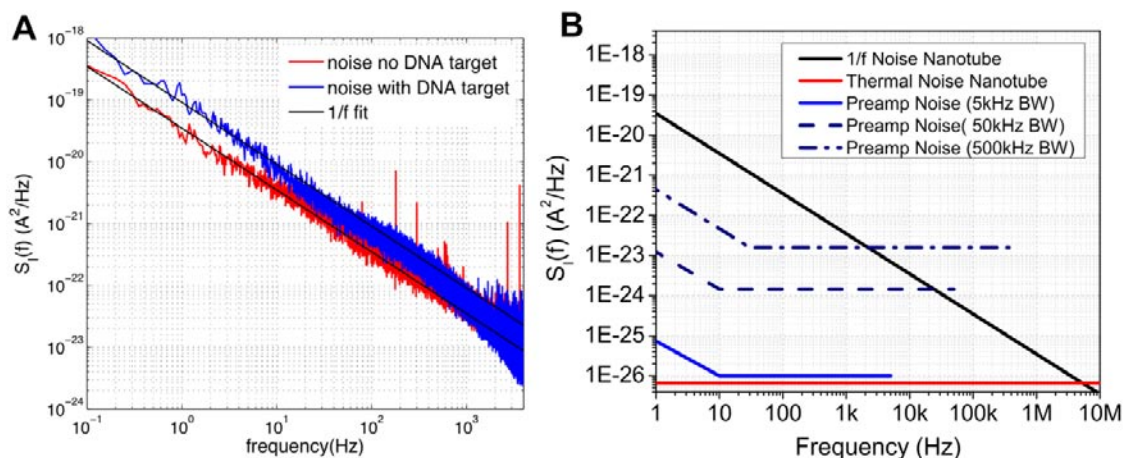


Figure S10. (A) Flicker noise for device shown in Fig. 2 with and without target at 31.9°C. (B) System level noise characterization.

The carbon nanotube noise at low frequencies is dominated by flicker (or $1/f$) noise, which can be seen from the measured power spectrum in Fig. S10A (calculated from the Fourier transform of the autocorrelation function). This background $1/f$ noise is higher in the presence of target DNA. The signal is determined by the conductance difference between the two peaks in Fig. 2. The noise is determined by integrating the noise spectrum from $f_{\text{lower}} = 1/T_{\text{window}}$ (where $T_{\text{window}}=30\text{s}$ is the length of the analyzed time window) and f_{upper} , the bandwidth established by the measurement equipment (approximately 4 kHz). The resulting SNR is shown in Table S1 as “SNR (from $1/f$)”. The noise can also be determined from the standard deviation of the Gaussian fits in Fig. 2, reported as “SNR (from σ)”. We find this noise floor to be slightly higher than the one computed from the integrated $1/f$ spectrum because of additional power supply noise harmonics, which are not integrated in the $1/f$ noise calculation. The SNR ratio can be improved by decreasing T_{window} (Fig. S11), since this results in a higher low-frequency cutoff, reducing the effect of low-frequency noise (drift). $T_{\text{window}}=15\text{s}$ is used for the Arrhenius plot fittings in Figs. 4d,e,f.

There is also noise coming from the measurement equipment, in this case the current preamplifier (Stanford Research SR570). As the bandwidth of the preamplifier is increased, the noise internally generated also increases, as shown in Fig. S10B (taken from the preamplifier’s datasheet). This noise, however, is significantly lower than that coming from the tube itself.

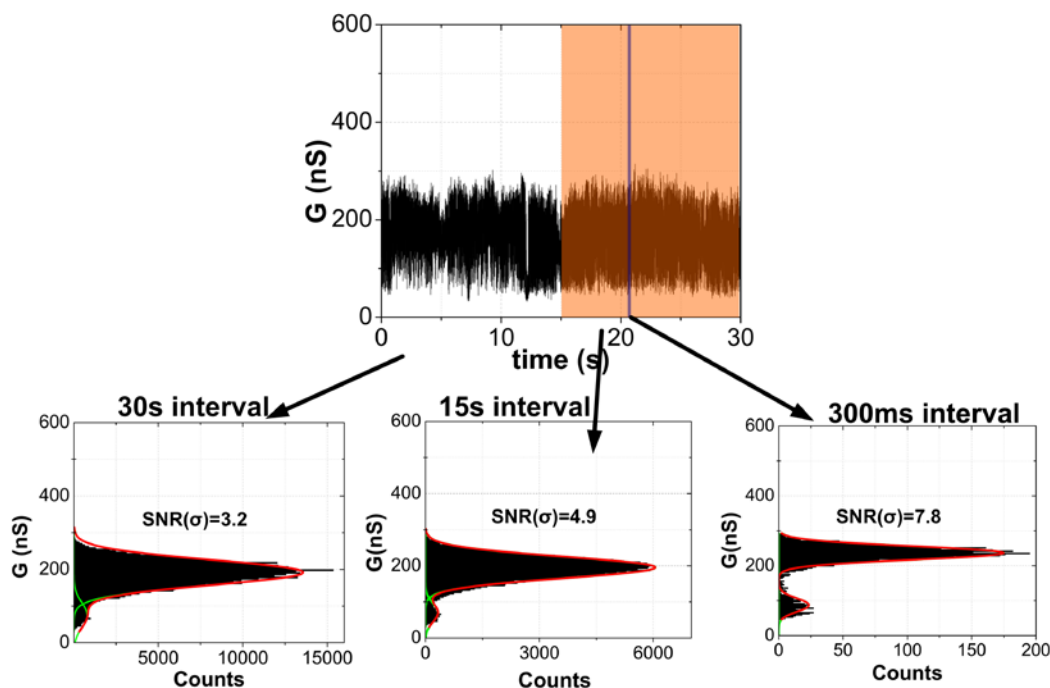


Figure S11. SNR(σ) for different time intervals

Noise Nanotube (pA_{rms})	998.4
Noise Preamp (pA_{rms})	14.1
SNR (from $1/f$)	5.7 - 11.7
SNR (from σ)	3 - 5.3

Table S1 Noise calculations at 4 kHz bandwidth for $T_{\text{window}}=30\text{s}$.

10. Bandwidth of nanotube device

The bandwidth of the nanotube device itself is also limited by extrinsic parasitics. The equivalent circuit is shown in Fig. S12. Here, R_{CNT} is the resistance of the nanotube, R_p is the resistance in the leads (due to the resistivity of titanium), C is the capacitance from the leads to the substrate and C_p is the parasitic capacitance from source to drain lead through the electrolyte. We characterize the bandwidth of the device with the small-signal transfer function from a current source in parallel with the nanotube to the output ($I_{\text{OUT}}/I_{\text{AC}}$). This is a valid assumption since $R_{\text{CNT}} \gg R_p$ and the current source simply adds to the nanotube current (approximating the conductance fluctuations).

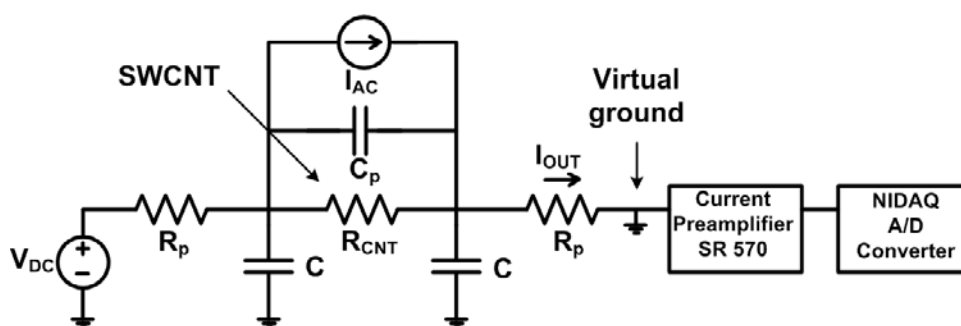


Figure S12. Small circuit equivalent model of nanotube device

We find that there are two poles $f_1 = \frac{1}{2\pi} \frac{2}{R_{\text{CNT}}} + \frac{1}{R_p} \frac{1}{2C + C_p}$ and $f_2 = \frac{1}{2\pi R_p C_p}$. Given our device geometry, $R_p \sim 5 \text{ k}\Omega$, $C_p \sim 2.1 \text{ nF}$, $C \sim 500 \text{ pF}$ and $R_{\text{CNT}} \sim 20 \text{ M}\Omega$, we find that $f_1 \sim 10 \text{ kHz}$ and $f_2 \sim 15 \text{ kHz}$. The bandwidth of the device can easily be improved by reducing these parasitics: we can grow the nanotubes on an insulating substrate (without the back gate), thereby reducing C ; the electrodes can be better passivated (with an oxide or resist) and

their size can be reduced so that C_p decreases; and we can use a different metal to reduce the series resistance R_p .

11. Ergodicity

The melting curves in Fig. 3a-c were extracted using Gaussian fits to the population histograms (Fig. 2B&S4). Because the observed binding kinetics are largely ergodic, this approximation is valid since the time average of the single molecule dynamics is equal to the ensemble average. However, the fluctuation lifetimes tend to have a distribution with a long tail (Fig S13A) from periods when the fluctuation process stops (up to a few seconds). When we include non-ergodic time intervals in the time average, the population histograms can be slightly skewed, resulting in a small shift of the melting curves (cf. Fig S13B and C).

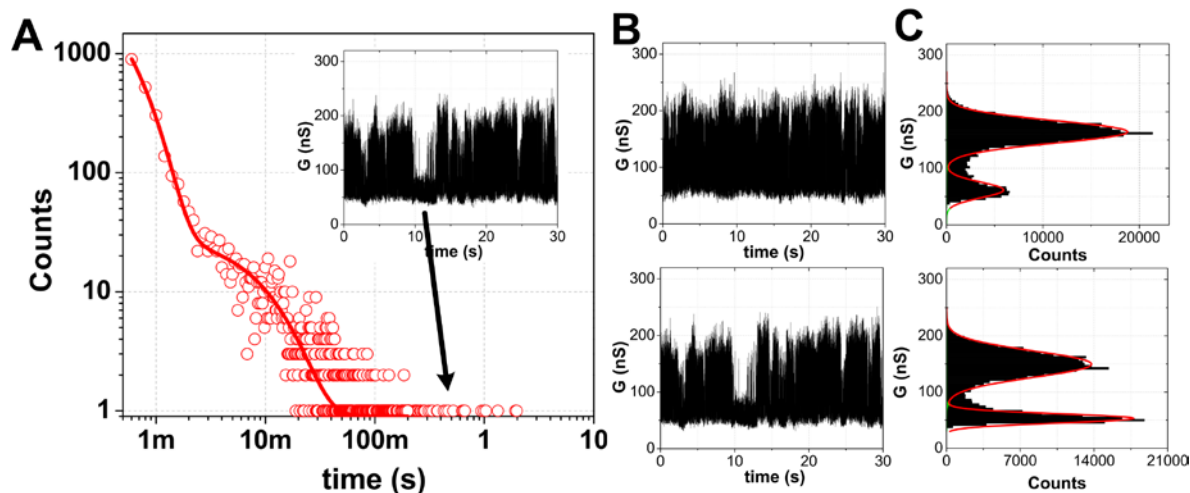


Figure S13. (A) Effect of non ergodic time intervals on the lifetime histogram (B) Effect of non ergodic time intervals on the conductance based histograms (taken at the same temperature)

12. Kinetic modes

The dwell time histograms for both DNA sequences over all measurements (temperature and target concentrations) can be best fit by a double exponential. This behavior originates from the system switching between two distinct kinetic modes (Fig. S14A is the same as that shown in Fig. 4b). We have identified and analyzed longer time intervals in which the system stays in only one of these modes. Fig. S14 B and C shows the dwell time histogram

at 1 μM DNA target concentration (Device 3), in which the system is in either the fast mode (total of three seconds) or slow mode (total of five seconds).

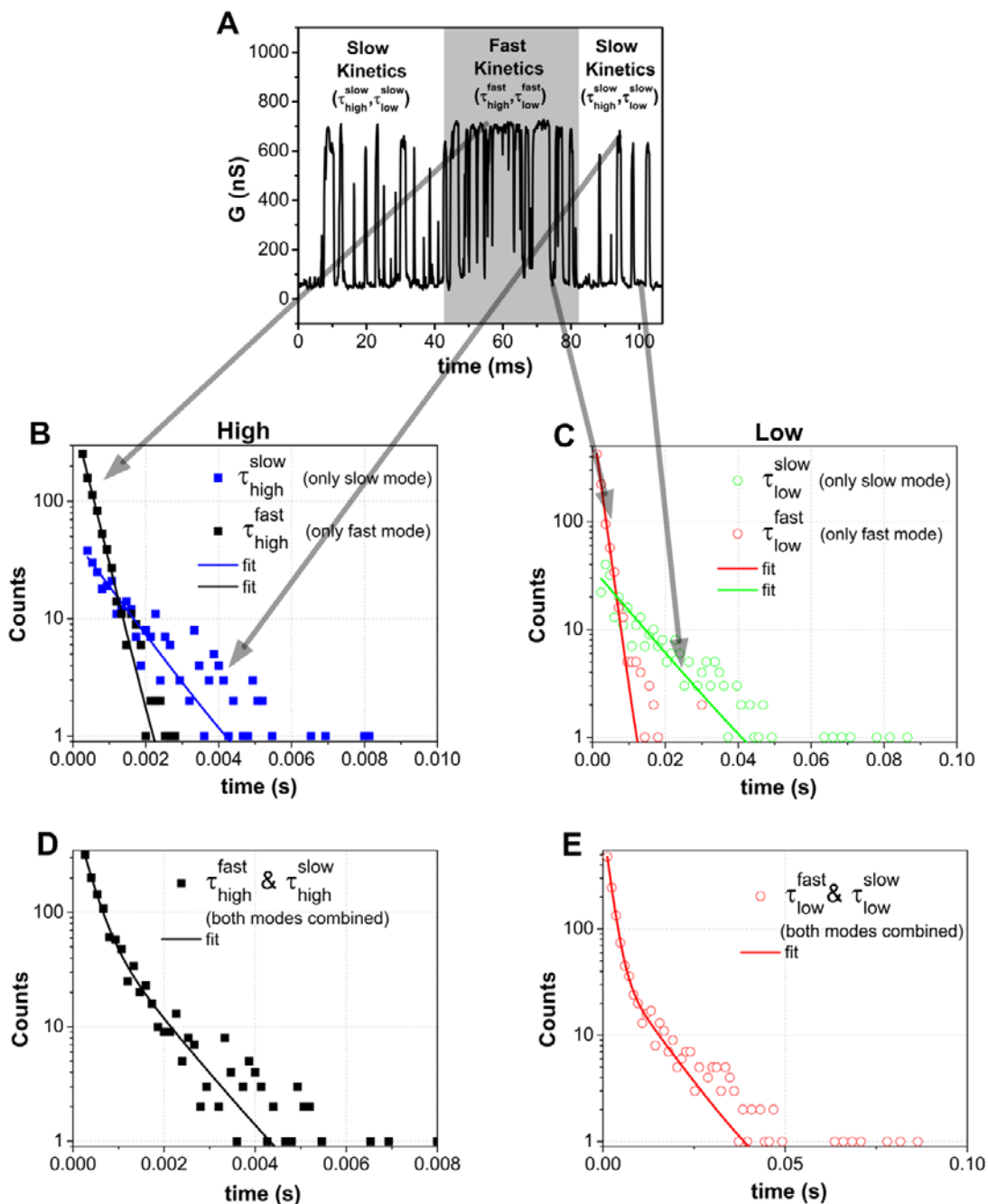


Figure S14. (A) Real time conductance data showing both surface and solution modes. (B,C) Dwell time histograms when modes are decoupled for high and low states. (D,E) Combined dwell time histograms when both modes are present leading to a double exponential.

When we analyze only a single mode, the dwell time histograms are largely mono-exponential and can be best fit with a single exponential function. This analysis also demonstrates that in the fast kinetic interval, both high and low lifetimes are shorter than in the slow kinetic interval. This behavior was seen over all temperatures and for both measured concentrations. When we analyze intervals with both modes present (Fig. S13 D and E), the dwell time histogram have a double exponential because of the combination of the fast and slow modes.

In Fig. 4d, we plot the Arrhenius plot for Device 3 corresponding to the solution mode, the expectations from solution-based DNA hybridization; the hybridization rate is proportional to concentration and the melting rate is independent of concentration. In Fig. S15, we show the Arrhenius plot for the surface mode for the same device. In this case, $k_{\text{hybridization}} = 1/\tau_{\text{high}}^{\text{slow}}$ and $k_{\text{melting}} = 1/\tau_{\text{low}}^{\text{slow}}$ for the 1 μM concentration and $k_{\text{hybridization}} = 1/\tau_{\text{high}}^{\text{fast}}$ and $k_{\text{melting}} = 1/\tau_{\text{low}}^{\text{fast}}$ for the 100 nM concentration. We believe that the surface mode is due to interactions of both the DNA duplex and the target with the carbon nanotube surface. This interaction should depend on many parameters such as the non-specific adsorption of DNA on nanotubes and the one-dimensional (1D) DNA diffusion rate along a nanotube. The behavior of the Arrhenius plot in Fig. S15 is consistent with a surface-based picture. The hybridization rate is mostly dependent on the 1D diffusion along the nanotube, which should be concentration independent². The melting is also dependent on the 1D diffusion but if there is more non-specific adsorption of DNA on the nanotube, there will be more negative charge along the nanotube, which will repel the bound target on the surface and make it more difficult to melt via the surface. We speculate that the concentration dependence of the surface melting rate should be inversely proportional to target concentration and the surface hybridization rate should be independent of concentration which roughly agrees with the Arrhenius plot in Fig. S15.

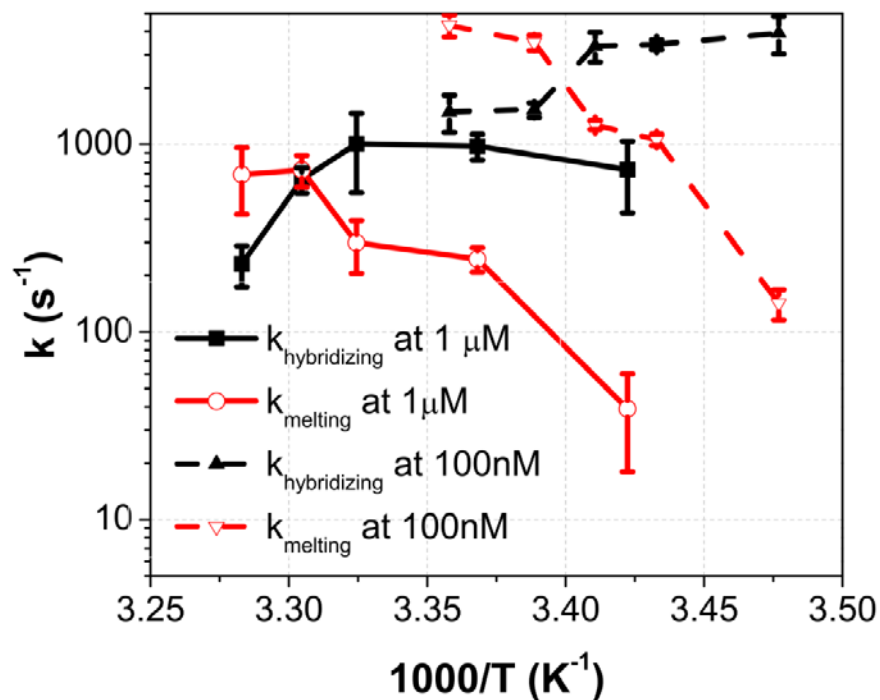


Figure S15. Arrhenius plot of surface based mode

References

1. Bronson, J.E., Fei, J., Hofman, J.M., Gonzalez, R.L., Jr. & Wiggins, C.H. Learning rates and states from biophysical time series: a Bayesian approach to model selection and single-molecule FRET data. *Biophys J* **97**, 3196-3205 (2009).
2. Halford, S.E. & Marko, J.F. How do site-specific DNA-binding proteins find their targets? *Nucleic Acids Res* **32**, 3040-3052 (2004).